The effects of chloride droplet properties on the underoil corrosion of API-X100 pipeline steel

Hongxing Liang,, *** Rebecca Filardo Schaller,* and Edouard Asselin.**

** Department of Materials Engineering, The University of British Columbia, Vancouver, BC, Canada.*

ARTICLE INFO (THIS STYLE IS ARTICLE AND ABSTRACT HEADING)

Article history:

Received Day Month Year (This style is Article History and Keywords)
Accepted Day Month Year
Available Day Month Year

Keywords:

A. Uniform corrosion
B. Chloride
C. Temperature
D. pH changes and effects
E. Cation

***Corresponding author: Hongxing Liang, telephone +001 6047739849; Department of Materials Engineering, The University of British Columbia, Frank Forward Building, 309-6350 Stores Road, Vancouver, BC, V6T 1Z4, Canada, email: (hongxingliang314@gmail.com).

"THIS IS A PREPRINT. THIS ARTICLE WAS PUBLISHED IN <Corrosion>.
DOI: <https://doi.org/10.5006/3152>"

ABSTRACT

The corrosive environment expected to form in diluted bitumen pipelines was explored by simulated exposure with a paraffin oil covered chloride droplet on API-X100 pipeline steel. The effects of droplet volume, chloride ion concentration, temperature, initial pH, and cation species on the underoil droplet corrosion behavior of API-X100 pipeline steel were studied by corrosion morphology and product identification combined with corrosion penetration measurements. The corrosion rate in the active region beneath the oil-covered sodium chloride droplets was inversely proportional to droplet volume but increased with increasing temperature and chloride ion concentration. Corrosion attack morphology was found to be dependent on initial droplet pH. At pH 2, uniform corrosion occurred across the entire area exposed under the oil-covered droplet. The oil-covered sodium chloride droplets with initial pH of 4 accelerated the uniform corrosion when compared to the droplet without initial pH control (pH ~ 5.5). However, at a high initial pH of 10, two active regions displaying different general corrosion rates and one inactive region were observed under the oil-covered droplet. At an even higher initial pH of 12, no obvious uniform corrosion was observed beneath the oil-covered droplet. Finally, in the exposures to droplets with varied cation, the uniform corrosion in the active region was reduced by either calcium or magnesium ions in the oil-covered droplet.

INTRODUCTION

It is reported that Canadian natural bitumen production will reach 4.5−5.8 million barrels per day by 2030.[1] Bitumen, which is usually diluted with a natural-gas condensate such as naphtha to reduce its viscosity, is primarily transported with pipelines.[2] Due to potential corrosion of the pipeline steels, separating water from bitumen is an important step in oil sand processing.[3] However, the separation process is usually not effective and some water droplets remain in the diluted bitumen (dilbit) after this process.[4] The water droplets in dilbit carry chlorides and may separate out onto pipe surfaces, which can cause internal corrosion of pipeline steels.[2] Factors that may influence the corrosion rates in these droplets include the droplet size, chloride concentration, temperature, initial pH, and the type of electrolyte, or cation present.

The water droplets, entrapped in the asphaltenes and clay particles that separate out from the dilbit, typically range from 100 to 1,000 µm in diameter.[5] These droplets may further accumulate on pipeline surfaces under certain circumstances, such as changes in flow patterns, and the diameters of the droplets can increase as a result.[6] Previously, Han, *et al.*,[7] examined a 6 µL 1.7 mM sodium chloride (NaCl) deaerated solution to simulate the possible droplets formed in a dilbit pipeline. In addition, many studies have investigated the corrosion of carbon steel [8-11] beneath chloride droplets with varying droplet size in the marine environment. The corrosion distribution of carbon steel beneath a macroscopic chloride droplet was explained by the Evans model which indicates the cathodic reaction is dominant around the edge of the droplet and the central part acts as an anode owing to differential diffusion of oxygen (O_2).[12] However, Li and Hihara [10] found that small NaCl droplets (diameter < ~100 µm) can passivate carbon steel owing to easy diffusion of O_2 to the corroded area whereas carbon steel was corroded actively beneath the larger droplets due to the Evans Cell formation (diameter > ~100 µm).

Freshwater is typically utilized in hot water extraction where bitumen can be separated from clay and sand.[13] The oil sand producers are required to store all process waters and tailings; the Cl^- concentration in the tailings ranges from 0.028 to 15.2 mM.[14] In order to reduce the use of freshwater, the oil sand producers recycle the tailings pond water. However, the concentration of Cl^- ions as well as the cations, such as calcium ions (Ca^{2+}) and magnesium ions (Mg^{2+}), of the process water increases with repeated recycling.[14] Some of the process water may enter the transmission pipelines at higher Cl^- and cation concentrations due to the recycling process resulting in higher chloride concentration droplets in the dilbit pipelines. The increase of Cl^- concentration has been found to accelerate the atmospheric corrosion rate of carbon steel under chloride droplets.[15] Further, according to Prosek, *et al.*,[16] the presence of either Mg^{2+} or Ca^{2+} could slightly increase the corrosion rate of carbon steel under atmospheric conditions.

As indicated in the literature,[2] under some circumstances, the transportation of dilbit is operated at the same temperatures as the shipment of other Canadian crude oils (4−25 °C). Additionally, elevated operation temperatures (60 °C) are used to increase the flow rate.[2] The variation of temperature may influence the oil-covered droplet corrosion rate of pipeline steel.

Initial droplet pH could also be a significant factor that governs corrosion under an oil-covered drop. In conventional bitumen extraction, an alkaline aqueous solution was mixed with bitumen in order to release natural surfactants from bitumen to the aqueous phase.[17] The typical water phase that may enter dilbit pipelines is in the pH range of ~7−9.[14] Recently, Jiang, *et al.*,[18] proposed a three-step

procedure to separate water, dilbit, and solids. In their third step, the pH of the mixture is reduced to 5.0 to separate diluted bitumen and the water phase. In this case, the water phase that may enter into the pipelines has a low pH. Our previous work also indicated that the under-oil droplet pH affected the formation of the active and inactive corrosion regions.[19] Some previous investigations have examined the relationship between initial pH and atmospheric corrosion behavior of iron[20] and carbon steel.[21] Nishikata, *et al.*,[20] reported that the effect of initial pH (3.0, 4.0, and 5.7) on the corrosion rate of iron beneath a thin chloride solution layer (thickness 10 μm to 1 mm) for 1 h was negligible, which was attributed to solution neutralization caused by corrosion reactions; in contrast to the under-oil droplets, under these exposure conditions there was a ready supply of oxygen. It was found by An, *et al.*,[21] that the corrosion rate of A3 carbon steel in simulated rain precipitation increased with the decreasing initial pH (5.7, 4.5, and 3.4) of simulated rainwater. Further investigation is necessary to establish the pH effect on the underoil droplet corrosion of pipeline steel in general, and X100 in particular.

In our previous works we established the corrosion mechanisms of chloride droplets under paraffin oil [19] and dilbit,[22] displaying a distinct corrosion mechanism from the traditional Evans droplet. However, the effects of droplet volume, Cl^- concentration, temperature, initial pH, and cation species on the oil-covered droplet corrosion behavior, including the corrosion products and corrosion attack morphologies, were not previously reported. In this study, a chloride droplet covered by paraffin oil is used to simulate the possible corrosive environments and factors influencing these droplets formed in dilbit pipelines. The results can be applied to predict corrosion rates that occur in droplets under oil coverings commonly observed in diluted bitumen transport pipelines.

Experimental

Materials

Table. 1 presents the chemical composition of the API-X100 pipeline steel investigated in this study. Rectangular specimens (10 × 10 × 6 mm) were cut from the API-X100 pipeline steel plate. The rectangular specimens were sequentially ground by silicon carbide papers of 120, 600, 1,200, and 2,000 grit.

Solutions and droplet corrosion

In the present study, droplet size was investigated for one chloride concentration (1.7 mM NaCl) and different volumes of 0.5 (~ 2,070 μm in diameter), 1 (~ 2,300 μm in diameter), 2 (~ 2,860 μm in diameter), and 5 (~ 3,660 μm in diameter) μL. The contact diameters between the droplets and specimens were obtained according to the corrosion product morphologies which were measured by scanning electron microscopy (SEM).

The effect of chloride ion concentrations was investigated for one droplet volume, 2 μL droplet, with concentrations of 1.7, 8.5, 17, and 85 mM NaCl. Conductivities of solutions with different NaCl additions were obtained using an Orion 105A+ conductivity meter (Thermo Electron Corporation). In addition, the influence of cations on the underoil droplet corrosion was studied. The calcium chloride ($CaCl_2$) solution (0.85 mM) and magnesium chloride ($MgCl_2$) solution (0.85 mM) with a 2 μL volume were prepared separately in order to obtain the same Cl^- concentration as the 1.7 mM NaCl droplet.

The pH range in this study will be 2−12. The 2 μL 1.7 mM NaCl droplets with initial pHs of 2, 4, 10, and 12 were prepared by the addition of perchloric acid ($HClO_4$, VWR) or sodium hydroxide (NaOH, Anachemia) in order to study the effect of initial pH on the oil-covered droplet corrosion. Although such extreme pH values (2 and 12) are not expected in dilbit pipelines, the effect of pH was conducted with an extended range to better understand the acidified anodic and basic cathodic regions that develop within the droplets.

The initial O_2 contents of all solutions at 23 °C were measured by an Extech 407510 oxygen meter (Extech Instruments). The average value of the different solutions was 0.269 ± 0.002 mM (8.582 ± 0.064 ppm). The pH values of all solutions were measured by an ALpHA® series epoxy electrode manufactured by OMEGA. The unadjusted pH of the solutions of 1.7–85 mM NaCl was 5.5 ± 0.1. The pHs of the 0.85 mM $CaCl_2$ and 0.85 mM $MgCl_2$ solutions were 5.5 ± 0.1 and 5.3 ± 0.1, respectively. The specimens, with the micropipetted droplets, were put in a jacketed cell. The water that circulated through the jacketed cell is connected with a water bath (temperature accuracy of ±1 °C). The jacketed cell was filled with paraffin oil (VWR analytical grade) to a thickness of 40 mm to completely cover the salt droplet. All specimens were exposed to the droplets for 14 h at 23 °C. The specific gravity and dynamic viscosity of paraffin oil at 23 °C are about 0.86 and 32 cSt, respectively. The density of paraffin oil at 20 °C is 0.872 g/cm^3. This is corroborated by Han et al. who have successfully used similar methods to simulate the corrosive environment in dilbit pipelines.[7] The sample was removed and the remaining paraffin oil and droplet were removed by a reagent-grade ethyl alcohol. The corrosion products were removed according to the ASTM G1−03 standard.[23] The descaling liquid used was hydrochloric acid (HCl, ACS reagent) solution (volume ratio 1:1) + 0.025 M methenamine ($(CH_2)_6N_4$, Anachemia). Each droplet deposition experiment under one of the above conditions was repeated a minimum of three times to ensure consistency.

The temperatures in this study will be set at 23 and 60 °C.[2] For evaluation of temperature effects, a 1.7 mM NaCl droplet with the volume of 2 μL was placed on the X100 under paraffin oil for 6 h at 60 °C. The relatively short measurement duration (6 h) was selected because the specimen corrosion was fast at 60 °C. For comparison, a second experiment was conducted with the same droplet size, concentration, and exposure time at 23 °C. The droplet deposition experiment at different temperatures was repeated a minimum of three times.

Surface morphology and microstructure characterization

The morphology of the corrosion products formed in different regions under the chloride droplets was characterized by a field-emission SEM (Zeiss Σigma) with an accelerating voltage of 20 kV. The high magnification SEM measurements were repeated at three different positions in the selected zones to ensure consistent results.

After corrosion product removal, the corrosion attack morphologies were characterized by SEM and profilometry. The areas of different regions in the SEM images were calculated using digital imaging software (Adobe Photoshop CS4, Adobe Systems Inc., US).

The three-dimensional morphology of the corrosion attack beneath the corrosion products was quantified using a surface profilometer (Dektak XT, Bruker) with a sub-nm resolution in the Z axis. For all profilometry measurements, the stylus force was adjusted to 1 mg. The scan area was determined by the droplet area. The volume loss of the active region beneath the oil-covered droplet for each test condition was determined by profilometry. The corrosion rate in the active region was then calculated based on the empirical equation for corrosion rate determination from volume loss:[24]

$$CR = \Delta V / At \quad (1)$$

where CR, ΔV, A, and t are the corrosion rate (mm/y) in the active region, the volume loss (mm^3) in the active region, the area (mm^2) of the active region, and the exposure time (y), respectively.

Results

The effect of droplet volume

Figure 1(a, b, c, and d) shows the SEM images of corrosion products formed during 14 h exposure under 1.7 mM NaCl droplets with volumes of 0.5, 1, 2, and 5 µL beneath paraffin oil. The resultant corrosion product displays two distinct regions of corrosion attack, labeled in Figure 1, with region 1 representing less aggressive attack (inactive region) and region 2, distinctly more aggressive attack (active region).

The corrosion attack morphologies post corrosion product removal are presented in Figure 2. Figure 2 also shows the two distinct areas: an inactive region (corresponding to region 2 in Figure 1) and an active region (corresponding to region 1 in Figure 1). High magnification SEM images of both the active and inactive regions are given in Figure 2. When the droplet volume is larger (2 or 5 µL), scratches from abrasion during specimen preparation are still apparent post corrosion in the active region. However, under smaller droplets (0.5 or 1 µL), the dissolution of the matrix was so fast that no scratches could be identified in the active region. This implied that the corrosion severity of the active region beneath the underoil droplet increased with decreasing droplet volume.

Profilometry measurements of the corrosion attack morphology due to exposure under the 1.7 mM NaCl droplets with varying volumes are shown in Figure 3. Some pitting can be identified in the inactive regions, while the active regions display general corrosion. The profilometry measurements give corrosion rates in the active regions for the droplets of 0.5, 1, 2, and 5 µL in volume of 0.635 ± 0.029, 0.550 ± 0.034, 0.463 ± 0.009, 0.412 ± 0.004 mm/y, respectively. The corrosion rate of the active region increased with reduced droplet volume.

The effect of Cl^- concentration

SEM characterization of the corrosion products formed on specimens exposed under oil covered 2 µL droplets with Cl^- concentrations of 1.7, 8.5, 17, and 85 mM for 14 h at 23 °C are shown in Figure 4. The inhomogeneous distribution of the resultant corrosion products is observed with similar distinction of active and inactive regions.

Figure 5 shows the corrosion attack that occurred beneath the four droplets after the removal of the corrosion products. Some pitting is observed in the inactive regions, whereas the active regions experienced general corrosion. Profilometry measurements of the corrosion attack morphology show corrosion rates in the active regions under the 1.7, 8.5, 17, and 85 mM NaCl droplets of 0.463 ± 0.009, 0.517 ± 0.024, 0.563 ± 0.018, and 0.596 ± 0.014 mm/y, respectively, indicating that the corrosion rate of the active region increased with increasing Cl^- concentration.

The effect of temperature

The morphology of the corrosion products formed under the 2 µL NaCl droplets at 23 °C and 60 °C for 6 h is shown in Figure 7(a and b), respectively. At 23 °C, the inactive region has fine-plate and rose type lepidocrocite and hexagonal hematite, whereas the active region consists of goethite, fine-plate and rose-type lepidocrocite as well as circular and hexagonal hematite (see supplementary information). At 60 °C, irregular elliptical hematite is seen in both the active and inactive regions (see supplementary information).

The corrosion attack after removal of the corrosion products is shown in Figure 8. At 23 °C, the abrading scratches from specimen preparation were still observed in Figure 8(c), while the surface in Figure 8(f) at 60 °C was corroded. The average corrosion depth of the active regions at different temperatures was also evaluated by profilometry (Figure 9). The corrosion rates of the active regions under the two droplets at 23 and 60 °C are 0.332 ± 0.070 and 1.329 ± 0.054 mm/y, respectively. The increase in temperature resulted in a significant increase in the corrosion rate of the active region.

The effect of initial pH

Figure 10 shows the corrosion product morphology formed beneath the oil-covered NaCl droplets of unmodified pH of 5.5 and initial pHs adjusted to 2, 4, 10, and 12. At an initial pH of 2, no separation of the active and inactive regions developed during droplet exposure (Figure 10(a)). The corrosion products under the NaCl droplet with an initial pH 4 (Figure 10(b)) show the division of the active and inactive regions similar to the unadjusted droplet. However, the corrosion products formed under the NaCl droplet with an initial pH of 10 consist of three distinct regions. The active region 1 in Figure 10(d) has more noticeable corrosion products with respect to the other two regions. At pH 12, no corrosion products were observed (Figure 10(e)).

Figure 11 presents the underlying corrosion attack for the API-X100 pipeline steel specimens exposed beneath the oil covered 2 µL 1.7 mM NaCl droplets with different pH values. Uniform corrosion occurred across the whole area exposed under the droplet with initial pH of 2 (Figure 11(a–c)). For pH 4, the active region in Figure 11(f) shows general corrosion, whereas pits can be identified in the inactive regions (Figure 11(e)). Under a high initial pH droplet, ≥ 10, no pits can be found in the inactive region (Figure 11(k)). Uniform corrosion occurred at both the active regions 1 (Figure 11(m)) and 2 (Figure 11(l)). No obvious uniform corrosion can be observed in the whole area under the oil-covered droplet at pH 12 (Figure 10(e and f)).

Profilometry measurement of the maximum corrosion depth in Figure 12(a) is −31.633 µm, much deeper than the maximum depths in Figure 12(b) (−9.989 µm), Figure 12(c) (−4.164 µm), and Figure 12(d) (−3.326 µm). The corrosion rates of the active regions for chloride droplets with initial pHs 2, 4, and 5.5 are 0.358 ± 0.004, 0.479 ± 0.020, and 0.463 ± 0.009 mm/y, respectively. The corrosion rate at pH 2 (0.357 ± 0.004 mm/y) is lower than that at pH 5.5 (0.463 ± 0.009 mm/y). However, the surface area of the uniformly corroded area at pH 2 (6.243 ± 0.083 mm^2) is larger than that of the active regions at pH 5.5 (2.617 ± 0.045 mm^2). The corrosion rates of the active regions 1 and 2 for chloride droplet with initial pH 10 are 0.505 ± 0.034 and 0.035 ± 0.001 mm/y, respectively.

The effect of the cation

The morphology of the corrosion products formed beneath the oil-covered droplets with different cations (Ca^{2+} and Mg^{2+}) are provided in Figure 13. After the corrosion products in Figure 13 were removed, the corrosion attack morphologies were imaged, Figure 14. For the specimen under 2 µL 1.7 mM NaCl droplet (Figure 14(a)), the area of the active region (2.720 ± 0.080 mm^2) is slightly smaller than that of the inactive region (3.846 ± 061 mm^2). In contrast, the area of the active region (4.119 ± 0.024 mm^2) in Figure 14(d) is larger than that of the inactive region (2.510 ± 0.079 mm^2). In addition, it was found that the inactive region under the $MgCl_2$ droplet was distributed along the edge of the droplet (Figure 14(g)). The presence of $MgCl_2$ in the oil-covered droplet significantly reduced the area of the inactive region (0.711 ± 0.080 mm^2) and increased the active region area (5.859 ± 0.050 mm^2), as indicated in Figure 14(g).

The variation in the corrosive environment established due to the different cations on the specimens is visible in Figure 15. In Figure 14(g), it is seen that the active region shows more corrosion penetration with respect to the inactive region. This is also corroborated by Figure 15(c). The corrosion rates are 0.463 ± 0.009, 0.325 ± 0.134, and 0.205 ± 0.012 mm/y, for the NaCl, $CaCl_2$, and $MgCl_2$ droplets, respectively. The corrosion rate of API-X100 underneath the

oil-covered droplet was reduced in the presence of either Ca^{2+} or Mg^{2+} in the oil-covered droplet.

Discussion

The effect of droplet volume

An inverse correlation between droplet volume and depth of uniform corrosion in the active region of the API-X100 pipeline steel was observed (Figure 3). It has been found that the variation in droplet size can influence droplet corrosion of carbon steels by governing the O_2 diffusion from the environment.[12] However, the replenishment rate of O_2 in paraffin oil is approximately two-thirds of that in water at 37 °C.[25] As a result, the limited supply of O_2 is controlled by diffusion through the paraffin oil and the small change of droplet size (5 to 0.5 µL) may not significantly affect the limited O_2 supply.

The following presents an explanation of the inverse correlation between droplet volume and uniform corrosion rate in the active region. The anodic and cathodic reactions of the specimen under a droplet are characterized by the iron (Fe) oxidation and O_2 reduction by:[26]

$$Fe = Fe^{2+} + 2e^- \quad (2)$$

$$H_2O + 1/2O_2 + 2e^- = 2OH^- \quad (3)$$

The ferric product formed under the oil-covered droplet may act as a cathode once oxygen is fully depleted.[27] According to reaction 2, ferrous ions (Fe^{2+}) could be produced as a result of the dissolution of the specimen. The hydrolysis of Fe^{2+} can cause H^+ production by:[28]

$$Fe^{2+} + H_2O = Fe(OH)^+ + H^+ \quad (4)$$

The Fe^{2+} will be oxidized to Fe^{3+} and the presence of Fe^{3+} can also lead to hydrolysis and H^+ production:[28]

$$Fe^{3+} + H_2O = Fe(OH)^{2+} + H^+ \quad (5)$$

$$Fe^{3+} + 2H_2O = Fe(OH)_2^+ + 2H^+ \quad (6)$$

$$2Fe^{3+} + 2H_2O = Fe_2(OH)_2^{4+} + 2H^+ \quad (7)$$

$$Fe^{3+} + 4H_2O = Fe(OH)_4^- + 4H^+ \quad (8)$$

The precipitation of $Fe(OH)_3$ is achieved by :[29]

$$Fe^{2+} + 2OH^- + (1/4)O_2 + (1/2)H_2O = Fe(OH)_3 \quad (9)$$

Based on this reaction, the formation of $Fe(OH)_3$ does not require additional alkali, because the oxygen reduction provides one hydroxide ion and the other two hydroxide ions are obtained from $Fe(OH)_2$. As a result, the oxidation of Fe^{2+} to $Fe(OH)_3$ would not affect the pH. The $Fe(OH)_3$ can dehydrate even in the presence of water and forms FeOOH by: [29]

$$Fe(OH)_3 = FeOOH + H_2O \quad (10)$$

In this reaction, no acid is consumed or generated, and there would be no change in pH. The following reaction can also occur:[28]

$$Fe(OH)_3 + 3H^+ = Fe^{3+} + H_2O \quad (11)$$

Finally, various crystal structures can be identified in the corrosion products (see supplementary information).

In a previous study on paraffin covered droplets, it was confirmed that the hydrolysis above the active region in the droplet led to the local formation of aggressive solutions with lower pH as corrosion developed.[19] In the inactive region, the cathodic reactions (reaction 3) caused a measurable pH rise.[19] Consistent with the previous study, the active region of the droplets showed the uniform corrosion due to the formation of aggressive solutions over the exposure period, while the inactive region still presented pitting (Figure 3). The cathodic reaction (reaction 3) accepted the electrons from the active region (reaction 2) to achieve charge balance. The Fe^{2+} produced by the dissolution of the steel in the smaller droplets might reach a sufficient level to cause precipitation (reaction 9) more quickly. As corrosion developed, the cathodic reaction (reaction 3) triggers the pH increase, while the hydrolysis of Fe^{2+} and Fe^{3+} (reactions 4, 5, 6, 7, and 8) can lead to the pH drop. Azmat, *et al.*, indicated that the "reservoir" of H^+ is relatively small and thus the pH shift would be more rapid for fine-sized acidified droplets (diameter < 5 µm) on the zinc surface.[30] The present work extends the inverse relationship between pH decrease and droplet size to the oil-covered macroscopic droplet. Details about the pH calculation for iron dissolution in NaCl solution are extensively documented in the literature [28] and a similar method was used to calculate the hydrogen ion concentration and corresponding pH value in the active region in this work. Similarly, we assume that the droplet volume above the active region is half of the total droplet volume and Fe^{2+} dissolved by the anodic reaction is immediately oxidized to Fe^{3+}. The calculated pHs for the 0.5, 1, 2, and 5 µL NaCl droplets after 14 h exposure are 3.4, 3.5, 3.7, and 3.9. Obviously, the calculated equilibrium pHs in the active regions increase with the increasing droplet volume. It should be noted that the real pHs should be higher than the calculated pHs due to the formation of corrosion products in the inactive regions and the possible occurrence of cathodic reaction in the active regions. Under the oil-covered droplets, it is postulated that the larger pH decrease in the active region accelerated the anodic dissolution of the API-X100 pipeline steel under smaller droplets. Therefore, the smaller droplet presented faster corrosion rate in the active regions, as shown in Figure 3.

The effect of Cl^- concentration

A positive correlation was established between the Cl^- concentration (1.7–85 mM) and uniform corrosion in the active region (Figure 6). It is reported that the increase of corrosion rate of iron in chloride solution with increasing NaCl concentration is due to enhanced solution conductivity.[24] The conductivity of the initial solution with different NaCl additions was measured. The initial solution conductivities of 1.7, 8.5, 17, and 85 mM NaCl solutions were 0.23 ± 0.01, 1.08 ± 0.01, 2.06 ± 0.01, 7.90 ±0.00 mS/cm. Higher conductivity leads to lower polarization with higher corrosion currents between adjoining anodes and cathodes. Furthermore, according to Kamimura, *et al.*,[28] the increased Cl^- activity in the active regions can contribute to an acceleration of the oxidation of Fe to Fe^{2+}. The hydrolysis reaction in the active region can also be accelerated by the accumulated Cl^- thus further decreasing pH.[28] Therefore, increased Cl^- concentration could accelerate corrosion in the active region.

The effect of temperature

The division of the inactive and the active region in the droplets was observed at two temperatures (Figure 8), implying that the temperatures in the range expected for dilbit pipelines studied here did not govern the corrosion mechanism, however, a dependence of

the corrosion penetration depth on temperature was observed. In general, temperature has been shown to significantly influence the corrosion rate of steel.[31] Based on Figure 9, the increase in temperature accelerated the corrosion severity in the active region. It is revealed that, even after 6 h, the corrosion rates (1.329 ± 0.054 mm/y) in the active regions of the specimens at 60 °C was greater than those (0.332 ± 0.070 mm/y) of the active regions formed at 23 °C. This can be related to the thermal activation of the electrochemical reactions.[32] In addition, the corrosion rate (0.332 ± 0.070 mm/y) after 6 h exposure is lower than that (0.463 ± 0.009 mm/y) after 14 h exposure, due to the longer portion of the total exposure time that the 14 h sample was subject to uniform corrosion.

The effect of initial pH

The corrosion morphology of API-X100 pipeline steel beneath the NaCl droplet was observed to be dependent on the initial droplet pH. Droplets exposed with an initial pH of 2 did not display the division of the active and inactive regions (Figure 11(a)). Uniform corrosion was found to occur across the whole area under the oil-covered NaCl droplet. According to the literature,[24] hydrogen evolution and oxygen reduction occur simultaneously in the droplet with an initial pH 2. Hydrogen reduction is the dominant cathodic reaction once oxygen is fully depleted. Once pH in the cathodes rises to above 4, the dominant cathodic reaction may be the reduction of ferric products if oxygen is completely depleted.[24] Due to the low initial pH (2), the pH rise caused by these cathodic reactions may not be sufficiently high to form an inactive region. Therefore, the whole area under the chloride with an initial pH of 2 presents uniform corrosion. It should be noted that the calculation of pH rise caused by oxygen reduction and hydrogen evolution through charge balance may not be feasible due to the possible reduction of ferric products. At an initial pH of 4, the formation of the active region and inactive regions occurred (Figure 11(d)). Compared with the droplet with an unmodified pH of 5.5 (Figure 12(c)), the NaCl droplets at pH 2 (Figure 12(a)) and 4 (Figure 12(b)) led to the formation of deeper pits. The formation of deeper pits might be associated with the initially low pH as lower pH (4) can trigger the formation of large pits in pipeline steel in bulk NaCl solution.[33] Moreover, the corrosion rate of the uniform corrosion in the active regions in Figure 12 (b and c) increased with the reduction of initial pH from 5.5 to 4. This has also been previously observed in bulk solution, where the uniform corrosion rate of mild steel in brine increased with the decreasing pH (from 13.5 to 1) at 24 °C.[34]

When the pH was increased above 5.5, again, a different corrosion morphology was observed. For an initial pH of 10, three distinct regions formed under the NaCl droplet (Figure 11(j)). At pH 10, after 3 h exposure (see supplementary information), the entire droplet area consists of one inactive region and one active region (formed in the initial area with pits). Again, the hydrolysis in the active region triggered the pH decrease, whereas the cathodic reactions (reaction 3) caused a measurable pH rise in the inactive region.[19] The initial pH in the inactive region of the oil-covered NaCl droplet is high and the cathodic reactions can be inhibited in the inactive region. After 5 h exposure (see supplementary information), a part (1.00 mm^2 in area) of the initial active region (2.60 mm^2 in area) transferred to the inactive region where the cathodic reactions occurred to accept the electrons from the active region and to sustain the corrosion dissolution. As a result, the initial active region was further separated into one active region (corresponding to active region 1 in Figure 11(j)) and one inactive region (corresponding to active region 2 in Figure 11(j)). The API-X100 pipeline steel was also exposed under an NaCl droplet with an initial high pH of 12 where no corrosion was observed under the entire area beneath the droplet. This is corroborated by Wang, *et al.*,[33] who stated that the location on X70 pipeline steel where Cl^- migrates to remains passive because of the lack of critical local chemistry for dissolution to occur if the pH of the chloride electrolyte is high enough (> 12).

The effect of the cation

The variation in cation type affected the area of corrosion attack under the droplet exposures on the API-X100 pipeline steel, where an inhibiting effect was observed in $MgCl_2$ or $CaCl_2$ as compared to NaCl. The areas of the inactive regions under the oil-covered 0.85 mM $CaCl_2$ (2.510 ± 0.079 mm^2) and $MgCl_2$ (0.711 ± 0.080 mm^2) droplets were smaller when compared with the inactive region area beneath the 1.7 mM NaCl droplet (3.846 ± 0.061 mm^2), as shown in Figure 14. Additionally, either Ca^{2+} or Mg^{2+} can inhibit the corrosion dissolution in the active region by reducing the corrosion rate. Precipitates containing calcium hydroxide ($Ca(OH)_2$) and magnesium hydroxide ($Mg(OH)_2$) were identified by SEM coupled with EDS in the inactive regions under the $CaCl_2$ and $MgCl_2$ droplets, respectively (see supplementary information). According to Blücher, *et al.*, the Mg^{2+} migrating to the cathodic sites led to a decrease of electrolytic conductivity and to the formation of an insulating $Mg(OH)_2$.[35] As a result, the $MgCl_2{\cdot}6H_2O$ decreased the chloride-induced atmospheric corrosion of aluminum. Moreover, they pointed out that in a concentrated aqueous solution of $MgCl_2$, $Mg(OH)_2$ precipitates if the pH is greater than 10. The pH in the inactive regions under the three droplets observed here was approximately 10, but for the $CaCl_2$ and $MgCl_2$ droplets these regions were reduced in size due to the precipitation of $Ca(OH)_2$ and $Mg(OH)_2$ (see supplementary information). With the presence of Ca^{2+} and Mg^{2+}, the available cathodic areas were reduced, while the anodic dissolution areas were enlarged. Lindström, *et al.*,[36] investigated the effect of chlorides and sulfates of sodium, magnesium, ammonium, and zinc on the corrosion of zinc exposed to a humid environment (relative humidity 95%) with 350 ppm carbon dioxide at 22 °C. It was revealed that the cathodic sites are blocked by the precipitation of hydroxide, oxide, or hydroxy salts and cannot serve as cathodes, leading to the inhibiting influence of Zn^{2+} and Mg^{2+} on zinc corrosion. Therefore, the cathodic reactions in the inactive region were inhibited due to the precipitation of $Ca(OH)_2$ and $Mg(OH)_2$ and resultant reduced cathodic areas. The inhibited cathodic reaction would reduce the possibility for electron acceptance from the active region where anodic dissolution of the API-X100 pipeline steel occurred. Consequently, the anodic dissolution depth in the active region of the $CaCl_2$ and $MgCl_2$ droplet was decreased.

Conclusions

The corrosion products and the corrosion attack morphologies of API-X100 pipeline steel exposed under a chloride droplet covered by paraffin oil simulating dilbit corrosion were investigated by varying the droplet volume, Cl^- concentration, temperature, pH, and cation type. The following key findings can be made:

- The uniform corrosion rate in the active region beneath the underoil NaCl droplet had an inverse correlation with droplet volume (0.5−5 µL) and a positive correlation with Cl^- concentration (1.7–85 mM) and temperature (23 and 60 °C).

- The corrosion morphology beneath the underoil 2 µL 1.7 mM NaCl droplet was shown to be dependent on initial droplet pH. At low initial pH, uniform corrosion occurred across the whole area exposed beneath the droplet and accelerated corrosion in the uniform corrosion regions was observed. At higher initial pH (10) the region under the droplet consisted of one inactive region and two distinct active regions. Finally, when the initial pH was increased even higher, to 12, no obvious uniform corrosion was observed under the droplet.

- The presence of either Ca^{2+} or Mg^{2+} (0.85 mM) in the oil-covered 2 µL droplet reduced the formation of the inactive region and the corrosion rate in the active region.

Acknowledgments

The financial support from the Natural Sciences and Engineering Research Council of Canada (NSERC) is acknowledged. Hongxing Liang expresses his gratitude to the China Scholarship Council for their financial support of his doctoral studies.

References

1. S.H. Mohr, G.M. Evans, *Energy Policy* 38, 1 (2010): p. 265-276.
2. "Effects of Diluted Bitumen on Crude Oil Transmission Pipelines," Transportation Research Board, Special report 311, 2013, p. 16-67.
3. Y. Xu, T. Dabros, H. Hamza, W. Shefantook, *Pet. Sci. Technol.* 17, 9-10 (1999): p. 1051-1070.
4. X. Wu, *Energy Fuels* 17, 1 (2003): p. 179-190.
5. M. Gray, Z. Xu, J. Masliyah, *Physics Today* 62, 3 (2009): p. 31-35.
6. J. Cai, C. Li, X. Tang, F. Ayello, S. Richter, S. Nesic, *Chem. Eng. Sci.* 73, (2012): p. 334-344.
7. D. Han, R. Jiang, Y. Cheng, *Electrochim. Acta* 114, (2013): p. 403-408.
8. B. Risteen, E. Schindelholz, R. Kelly, *J. Electrochem. Soc.* 161, 14 (2014): p. 580-586.
9. S. Li, L.H. Hihara, *Corros. Sci.* 108, (2016): p. 200-204.
10. S. Li, L. Hihara, J. Electrochem. Soc. 159, 11 (2012): p. 461-468.
11. S. Li, L. Hihara, *Corros. Eng. Sci. Techn.* 45, 1 (2010): p. 49-56.
12. U.R. Evans, The Corrosion and the Oxidation of Metals (New York, NY: St. Martins Press, 1960).
13. Q. Dai, K.H. Chung, Fuel 75, 2 (1996): p. 220-226.
14. E.W. Allen, *J. Environ. Eng. Sci.* 7, 2 (2008): p. 123-138.
15. T. Tsuru, K.I. Tamiya, A. Nishikata, *Electrochim. Acta* 49, 17 (2004): p. 2709-2715.
16. T. Prosek, D. Thierry, C. Taxén, J. Maixner, *Corros. Sci.* 49, 6 (2007): p. 2676-2693.
17. S. Gao, K. Moran, Z. Xu, J. Masliyah, *J.Phys.Chem.B.* 114, 23 (2010): p. 7710-7718.
18. T. Jiang, G.J. Hirasaki, C.A. Miller, K. Moran, *Energy Fuels* 22, 6 (2008): p. 4158-4164.
19. H. Liang, J. Liu, R. Schaller, E. Asselin, *Corrosion* 74, 9 (2018): p. 947-957.
20. A. Nishikata, Y. Ichihara, Y. Hayashi, T. Tsuru, *J. Electrochem. Soc.* 144, 4 (1997): p. 1244-1252.
21. B. An, X. Zhang, E. Han, H. Li, *J. Mater. Sci. Technol.* 20, 2 (2004): p. 220-222.
22. H. Liang, J. Liu, A. Alfantazi, E. Asselin, Mater. Lett. 222, (2018): p. 196-199.
23. ASTM G1-03, "Standard Practice for Preparing, Cleaning, and Evaluating Corrosion Test Specimens" (West Conshohocken, PA: ASTM International, 2011).
24. D.A. Jones, Principles and Prevention of Corrosion, 2nd ed. (Upper Saddle River, NJ: Prentice Hall, 1992).
25. Y.M. Stokes, *Mol. Reprod. Dev* 76, 12 (2009): p. 1178-1187.
26. N. Kıcır, G. Tansuğ, M. Erbil, T. Tüken, *Corros. Sci.* 105, (2016): p. 88-99.
27. V. Lair, H. Antony, L. Legrand, A. Chaussé, *Corros. Sci.* 48, 8 (2006): p. 2050-2063.
28. T. Kamimura, K. Kashima, K. Sugae, H. Miyuki, T. Kudo, *Corros. Sci.* 62, (2012): p. 34-41.
29. H. Tamura, *Corros. Sci.* 50, 7 (2008): p. 1872-1883.
30. N.S. Azmat, K.D. Ralston, B.C. Muddle, I.S. Cole, *Corros. Sci.* 53, 11 (2011): p. 3534-3541.
31. Y. Wang, G. Cheng, Y. Li, *Corros. Sci.* 111, (2016): p. 508-517.
32. M. Esmaily, M. Shahabi-Navid, J.E. Svensson, M. Halvarsson, L. Nyborg, Y. Cao, L.G. Johansson, *Corros. Sci.* 90, (2015): p. 420-433.
33. Y. Wang, G. Cheng, W. Wu, Q. Qiao, Y. Li, X. Li, *Appl. Surf. Sci.* 349, (2015): p. 746-756.
34. O. Riggs Jr, J. Sudbury, M. Hutchison, *Corrosion* 16, 6 (1960): p. 260-264.
35. D.B. Blücher, J.E. Svensson, L.G. Johansson, *Corros. Sci.* 48, 7 (2006): p. 1848-1866.
36. R. Lindström, J.E. Svensson, L.G. Johansson, *J. Electrochem. Soc.* 149, 2 (2002): p. 57-64.

FIGURE CAPTIONS

FIGURE 1. SEM secondary electron (SE) images of API-X100 pipeline steel specimens exposed under oil covered 1.7 mM NaCl droplets with volumes of 0.5 (a), 1 (b), 2 (c), and 5 (d) µL for 14 h at 23 °C.

FIGURE 2. SEM SE images of the underlying corrosion attack after removal of corrosion products on the API-X100 pipeline steel specimens exposed beneath the oil covered 1.7 mM NaCl droplets with volumes of 0.5 (a, b, and c), 1 (d, e, and f), 2 (g, h, and i), and 5 (j, k, and l) µL for 14 h at 23 °C.

FIGURE 3. The three-dimensional morphologies of the corrosion attack after removal of corrosion products formed beneath oil covered 1.7 mM NaCl droplets with volumes of 0.5 (a), 1 (b), 2 (c), and 5 (d) µL for 14 h at 23 °C.

FIGURE 4. SEM SE images of the corrosion morphology on API-X100 pipeline steel specimens exposed under 2 µL NaCl droplets covered in oil with Cl^- concentrations of 1.7 (a), 8.5 (b), 17 (c), and 85 (d) mM for 14 h at 23 °C.

FIGURE 5. SEM SE images of the underlying corrosion attack after removal of corrosion products on the API-X100 pipeline steel specimens exposed beneath the oil covered 2 µL NaCl droplets with Cl^- concentrations of 1.7 (a, b, and c), 8.5 (d, e, and f), 17 (g, h, and i), and 85 (j, k, and l) mM for 14 h at 23 °C.

FIGURE 6. The three-dimensional morphologies of the corrosion attack after removal of corrosion products formed beneath 2 µL NaCl droplets with Cl^- concentrations of 1.7 (a), 8.5 (b), 17 (c), and 85 (d) mM exposed under oil for 14 h at 23 °C.

FIGURE 7. SEM SE images of the corrosion morphology on API-X100 pipeline steel specimens exposed under oil covered 2 µL 1.7 mM NaCl droplets for 6 h at 23 °C (a) and 60 °C (b).

FIGURE 8. SEM SE images of the underlying corrosion attack after removal of corrosion products on the API-X100 pipeline steel specimens exposed beneath oil covered 2 µL 1.7 mM NaCl droplets for 6 h at 23 °C (a, b, and c) and 60 °C (d, e, and f).

FIGURE 9. The three-dimensional morphology of the corrosion attack after removal of corrosion products formed by exposure beneath oil covered 2 µL 1.7 mM NaCl droplets for 6 h at 23 °C (a) and 60 °C (b).

FIGURE 10. SEM SE images of API-X100 pipeline steel specimens exposed under oil covered 2 µL 1.7 mM NaCl droplets with initial pHs of 2 (a), 4 (b), 5.5 (c), 10 (d), and 12 (e and f) for 14 h at 23 °C.

FIGURE 11. SEM SE images of the underlying corrosion attack after removal of corrosion products on the API-X100 pipeline steel specimens exposed beneath the oil covered 2 µL 1.7 mM NaCl droplets

with initial pHs of 2 (a, b, and c), 4 (d, e, and f), 5.5 (g, h, and i), and 10 (j, k, l, and m) for 14 h at 23 °C.

FIGURE 12. The three-dimensional morphologies of the corrosion attack after removal of corrosion products formed beneath oil covered 2 µL 1.7 mM NaCl droplets with initial pHs of 2 (a), 4 (b), 5.5 (c), and 10 (d) for 14 h at 23 °C.

FIGURE 13. SEM SE images of API-X100 pipeline steel specimens exposed under oil covered 1.7 mM NaCl (a), 0.85 mM $CaCl_2$ (b), and 0.85 mM $MgCl_2$ (c) droplets with the volume of 2 µL for 14 h at 23 °C.

FIGURE 14. SEM SE images of the underlying corrosion attack after removal of corrosion products on the API-X100 pipeline steel specimens exposed beneath the oil covered 1.7 mM NaCl (a, b, and c), 0.85 mM $CaCl_2$ (d, e, and f), and 0.85 mM $MgCl_2$ (g, h, and i) droplets with the volume of 2 µL for 14 h at 23 °C.

FIGURE 15. The three-dimensional morphologies of the corrosion attack after removal of corrosion products formed beneath oil covered 1.7 mM NaCl (a), 0.85 mM $CaCl_2$ (b) and 0.85 mM $MgCl_2$ (c) droplets with the volume of 2 µL for 14 h at 23 °C.

TABLE CAPTIONS

TABLE 1. Chemical composition of the API-X100 pipeline steel specimens.

Figures

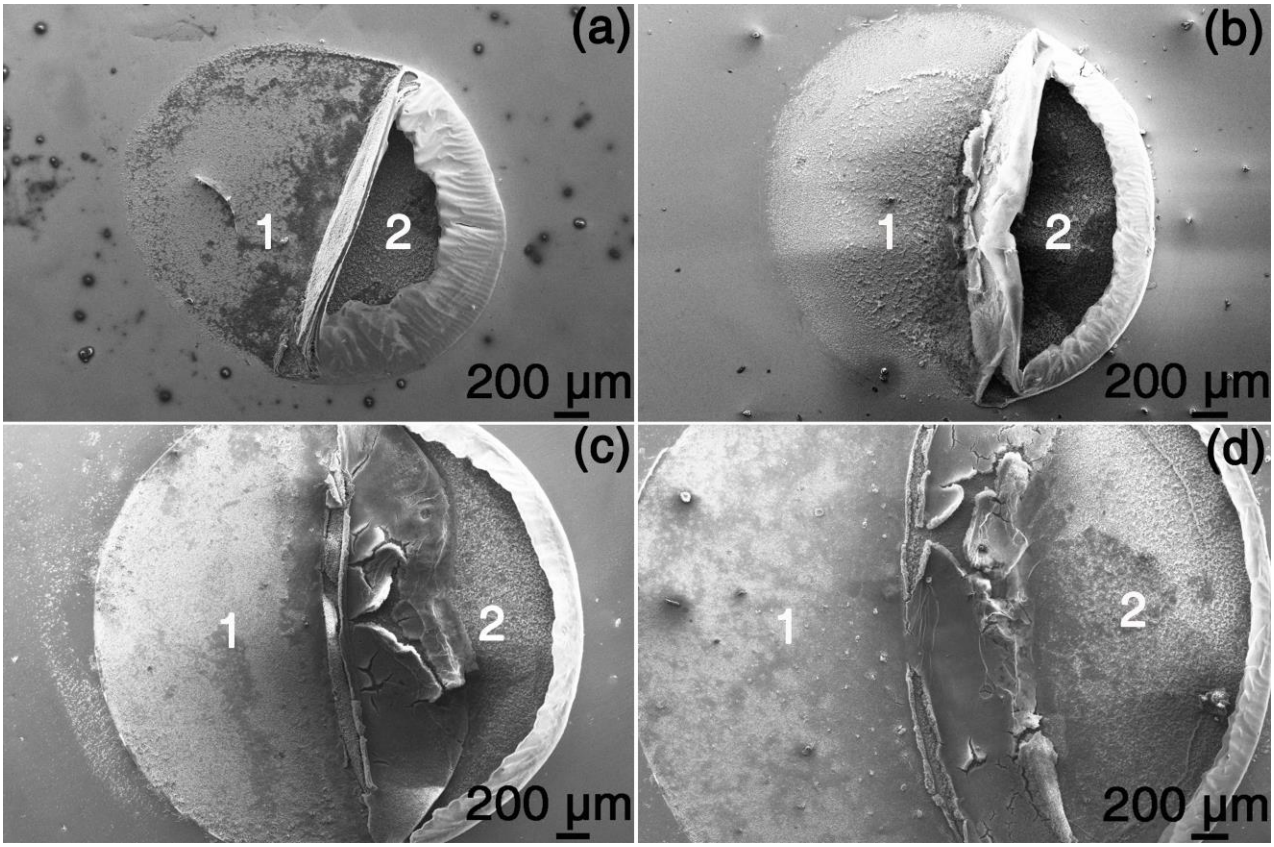

FIGURE 1. SEM secondary electron (SE) images of API-X100 pipeline steel specimens exposed under oil covered 1.7 mM NaCl droplets with volumes of 0.5 (a), 1 (b), 2 (c), and 5 (d) µL for 14 h at 23 °C.

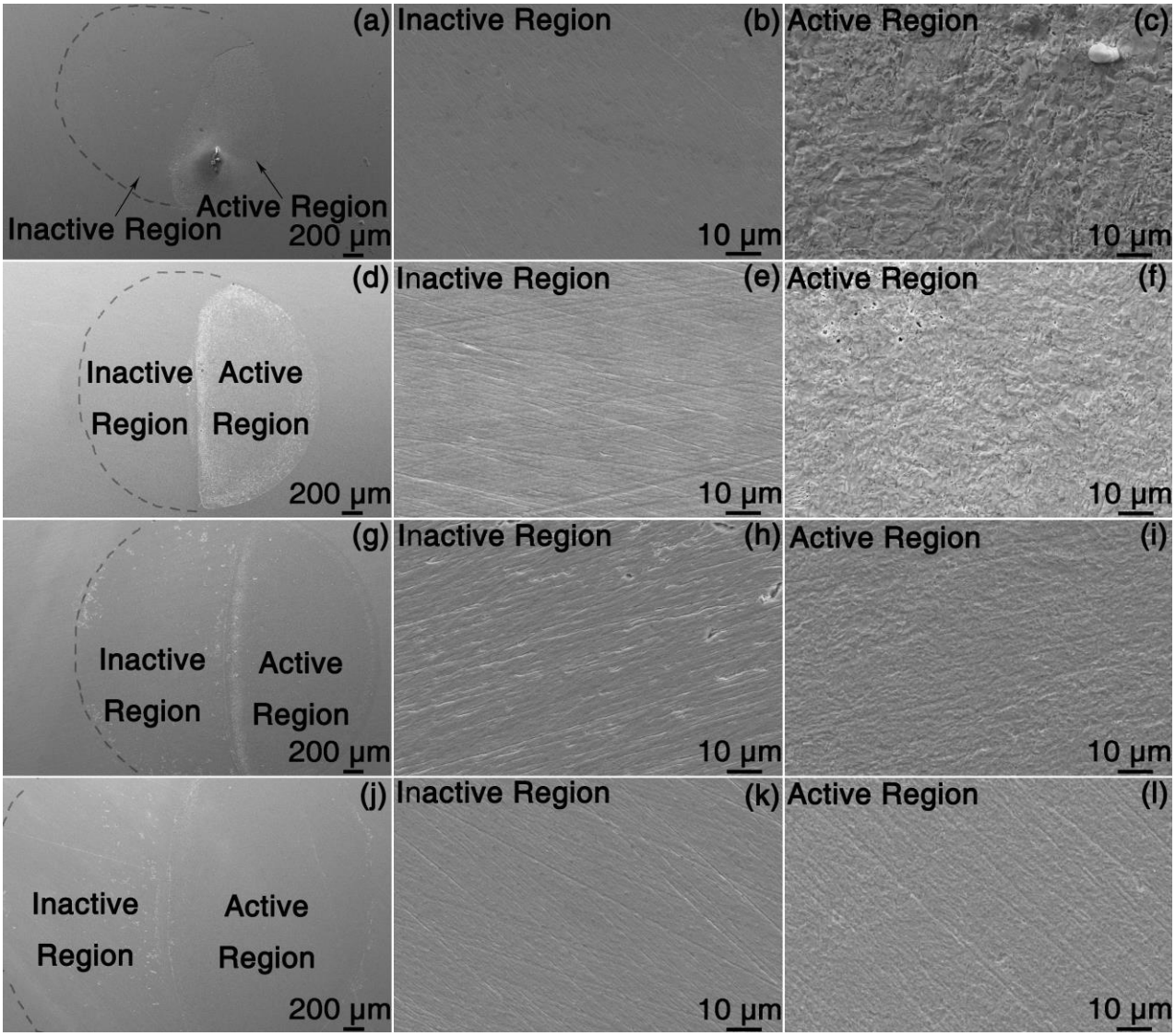

FIGURE 2. SEM SE images of the underlying corrosion attack after removal of corrosion products on the API-X100 pipeline steel specimens exposed beneath the oil covered 1.7 mM NaCl droplets with volumes of 0.5 (a, b, and c), 1 (d, e, and f), 2 (g, h, and i), and 5 (j, k, and l) µL for 14 h at 23 °C.

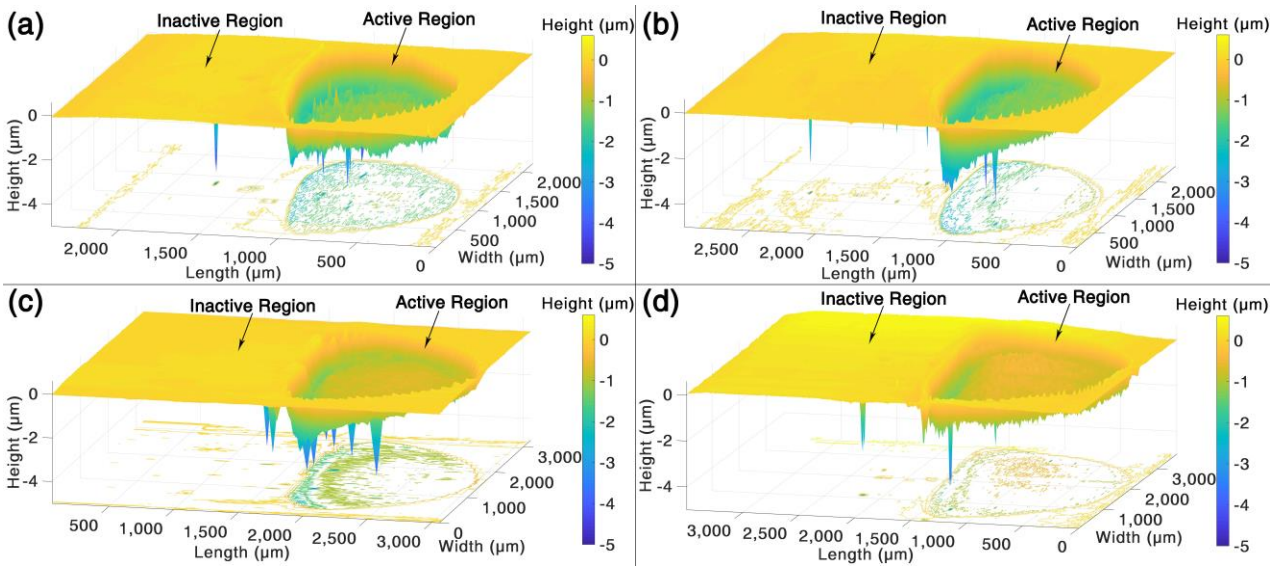

FIGURE 3. The three-dimensional morphologies of the corrosion attack after removal of corrosion products formed beneath oil covered 1.7 mM NaCl droplets with volumes of 0.5 (a), 1 (b), 2 (c), and 5 (d) µL for 14 h at 23 °C.

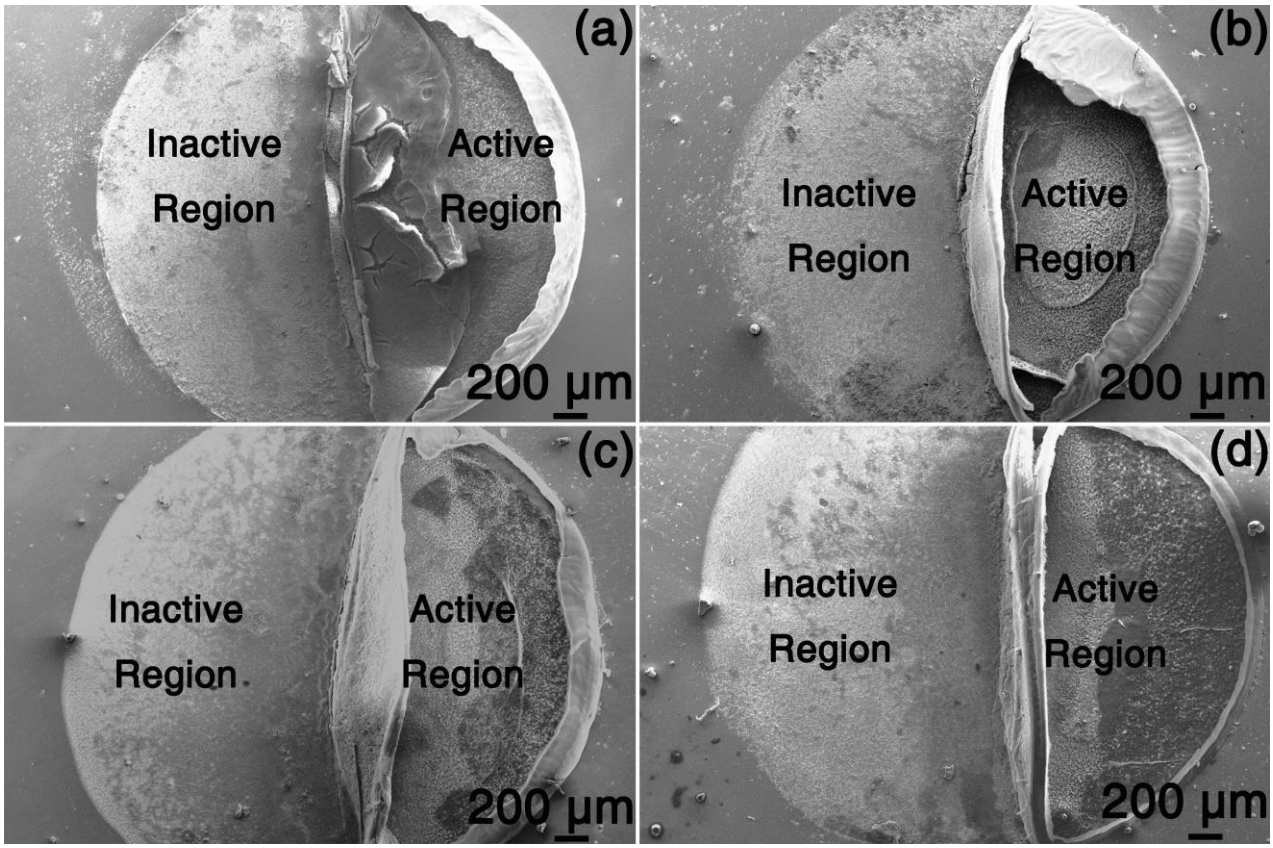

FIGURE 4. SEM SE images of the corrosion morphology on API-X100 pipeline steel specimens exposed under 2 µL NaCl droplets covered in oil with Cl^- concentrations of 1.7 (a), 8.5 (b), 17 (c), and 85 (d) mM for 14 h at 23 °C.

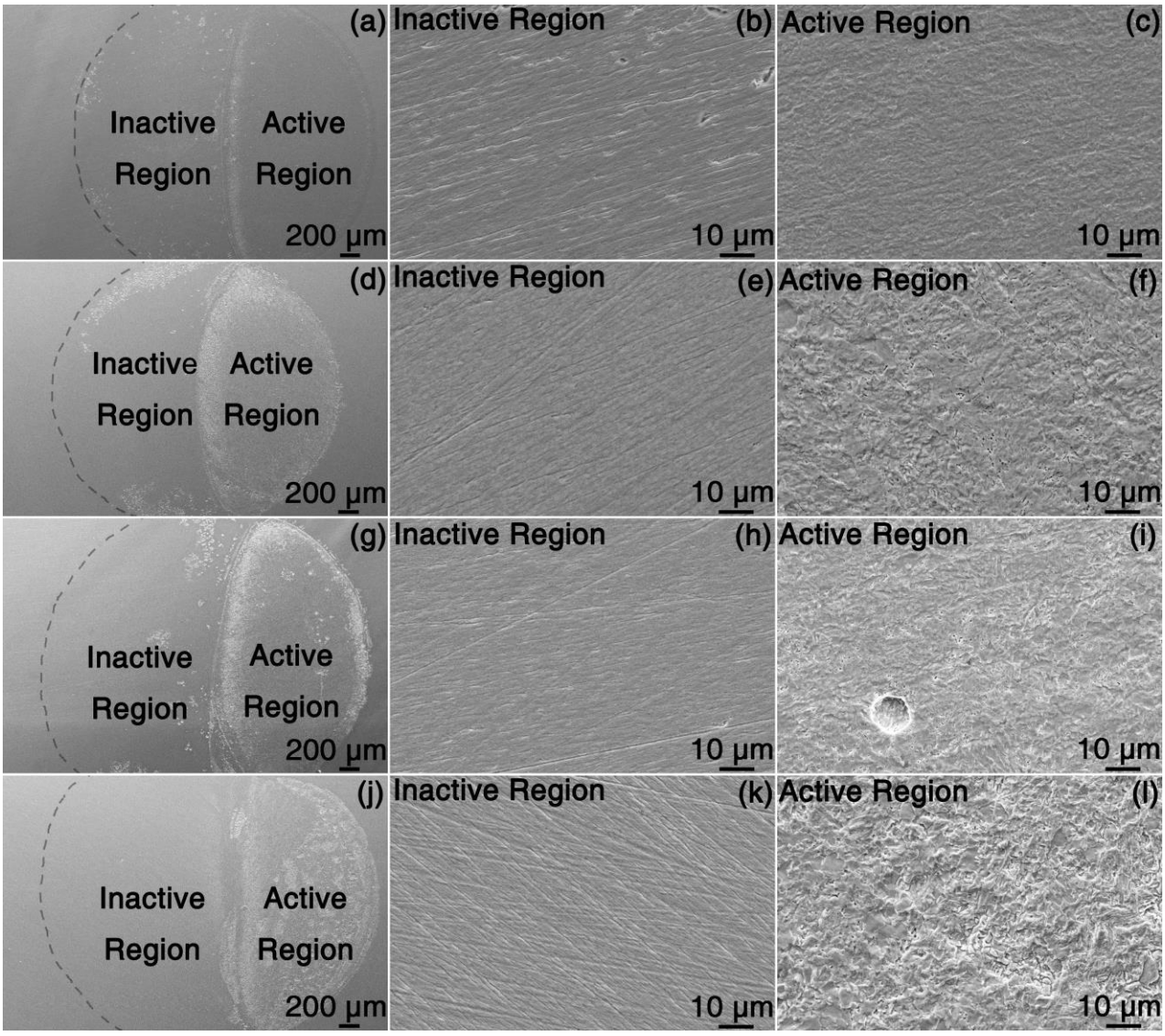

FIGURE 5. SEM SE images of the underlying corrosion attack after removal of corrosion products on the API-X100 pipeline steel specimens exposed beneath the oil covered 2 µL NaCl droplets with Cl^- concentrations of 1.7 (a, b, and c), 8.5 (d, e, and f), 17 (g, h, and i), and 85 (j, k, and l) mM for 14 h at 23 °C.

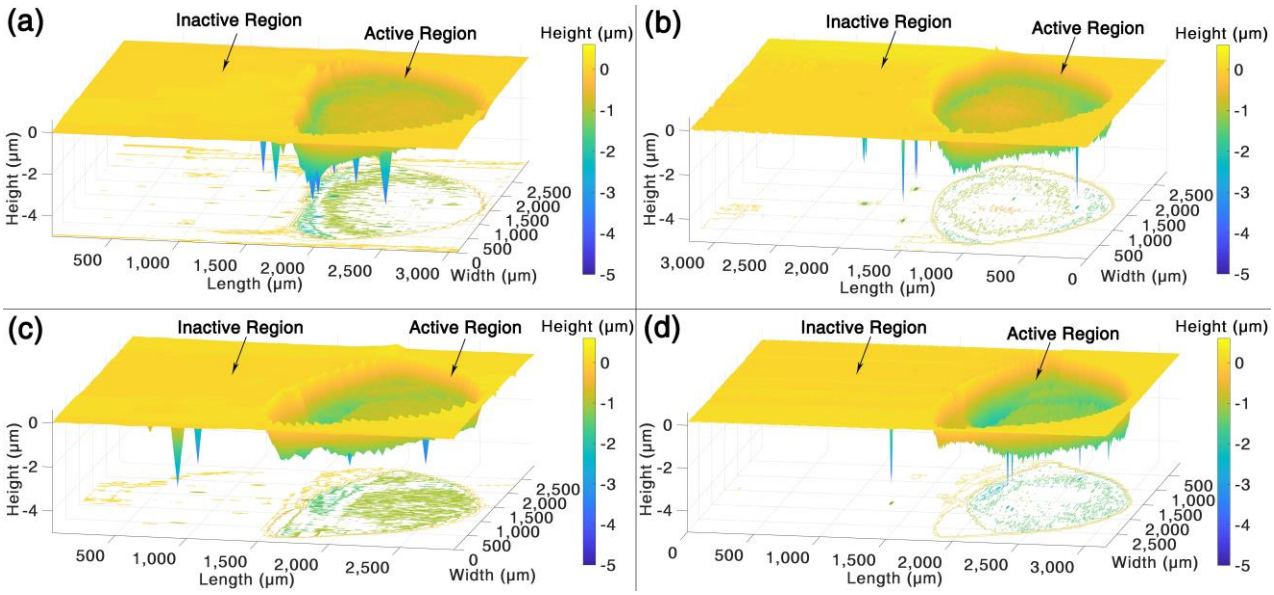

FIGURE 6. The three-dimensional morphologies of the corrosion attack after removal of corrosion products formed beneath 2 µL NaCl droplets with Cl^- concentrations of 1.7 (a), 8.5 (b), 17 (c), and 85 (d) mM exposed under oil for 14 h at 23 °C.

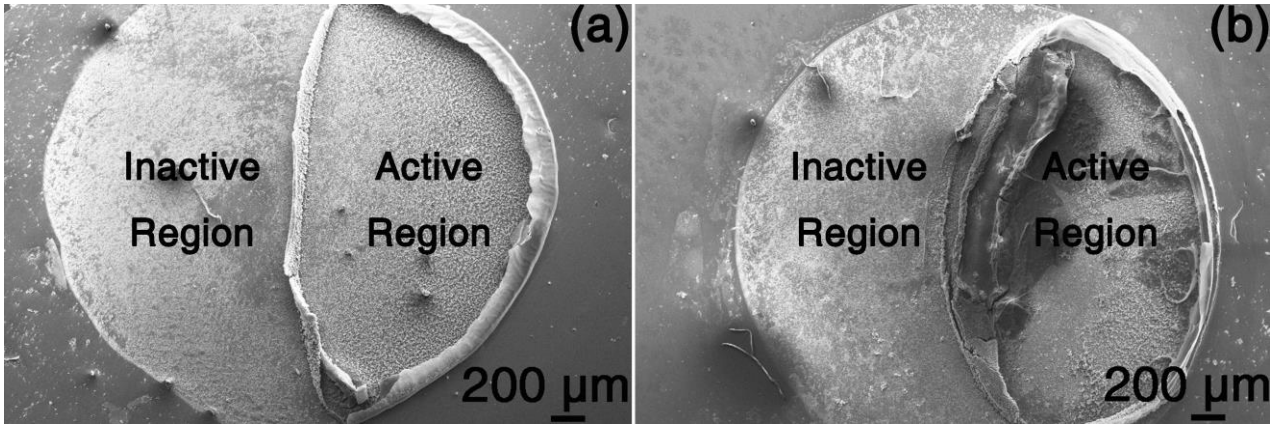

FIGURE 7. SEM SE images of the corrosion morphology on API-X100 pipeline steel specimens exposed under oil covered 2 µL 1.7 mM NaCl droplets for 6 h at 23 °C (a) and 60 °C (b).

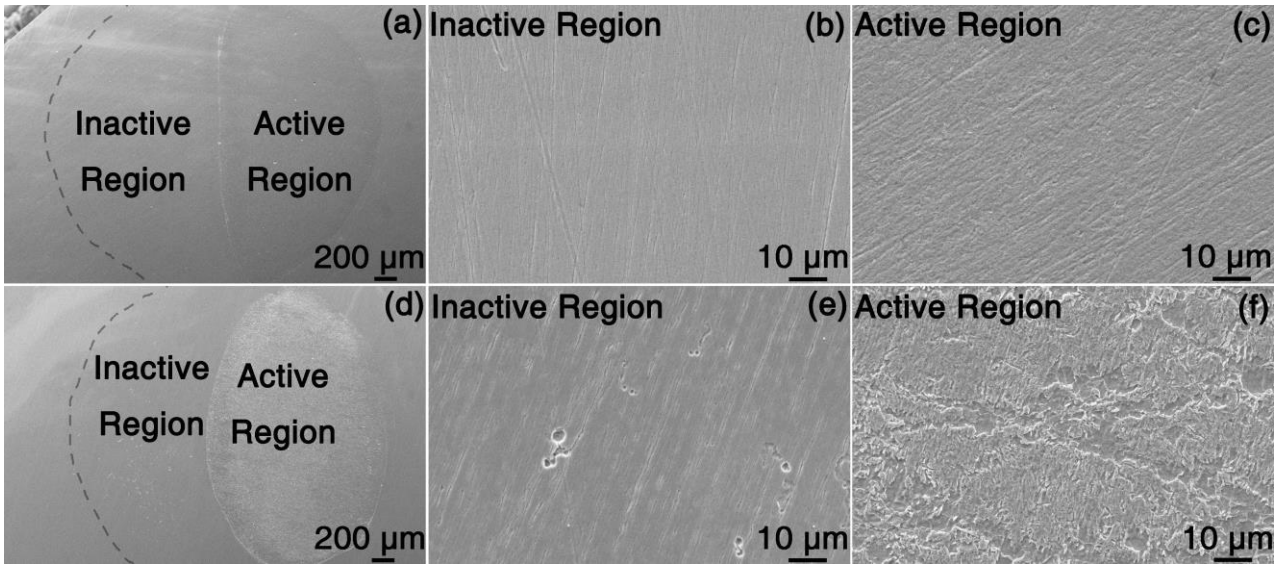

FIGURE 8. SEM SE images of the underlying corrosion attack after removal of corrosion products on the API-X100 pipeline steel specimens exposed beneath oil covered 2 µL 1.7 mM NaCl droplets for 6 h at 23 °C (a, b, and c) and 60 °C (d, e, and f).

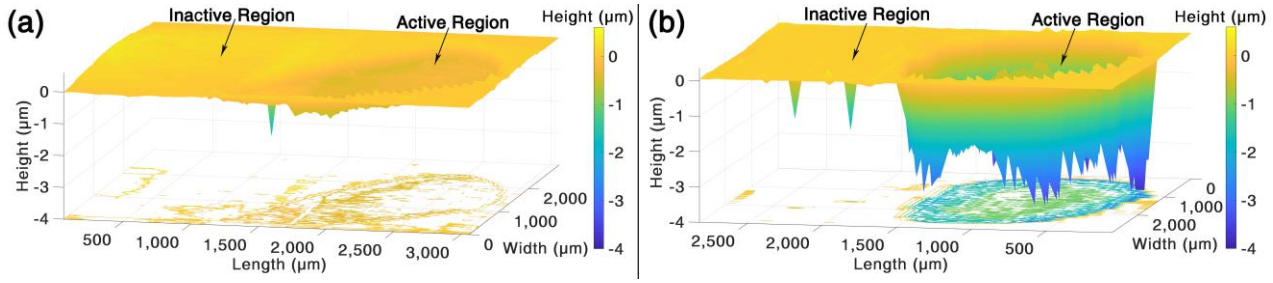

FIGURE 9. The three-dimensional morphology of the corrosion attack after removal of corrosion products formed by exposure beneath oil covered 2 µL 1.7 mM NaCl droplets for 6 h at 23 °C (a) and 60 °C (b).

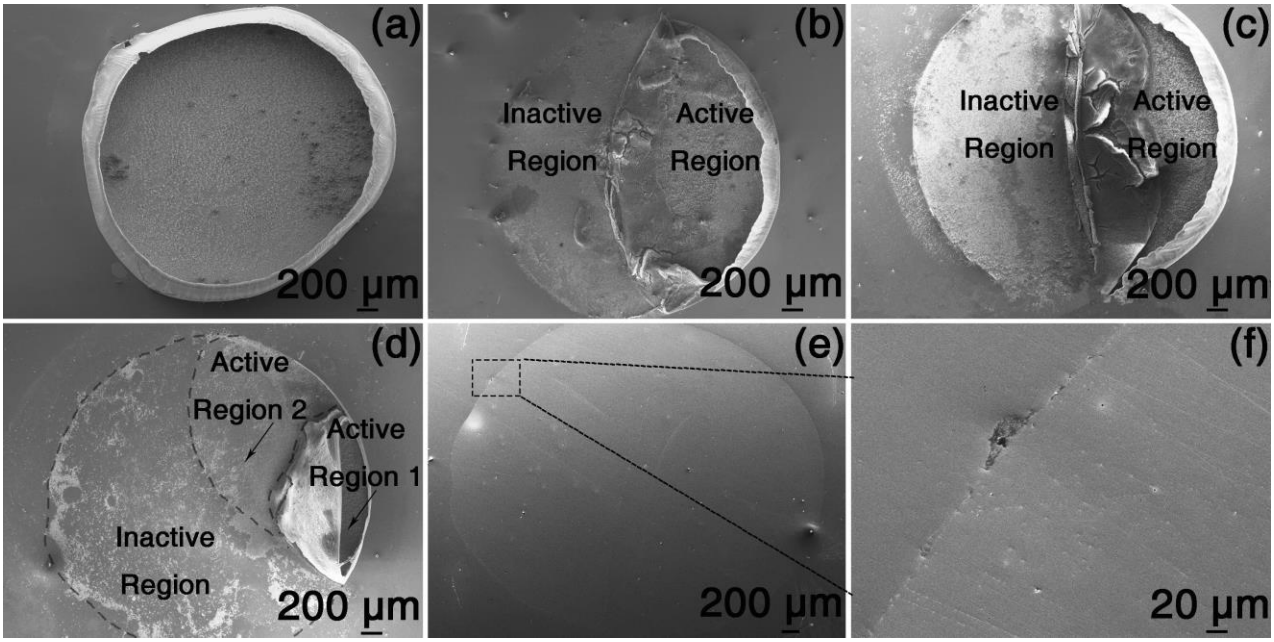

FIGURE 10. SEM SE images of API-X100 pipeline steel specimens exposed under oil covered 2 µL 1.7 mM NaCl droplets with initial pHs of 2 (a), 4 (b), 5.5 (c), 10 (d), and 12 (e and f) for 14 h at 23 °C.

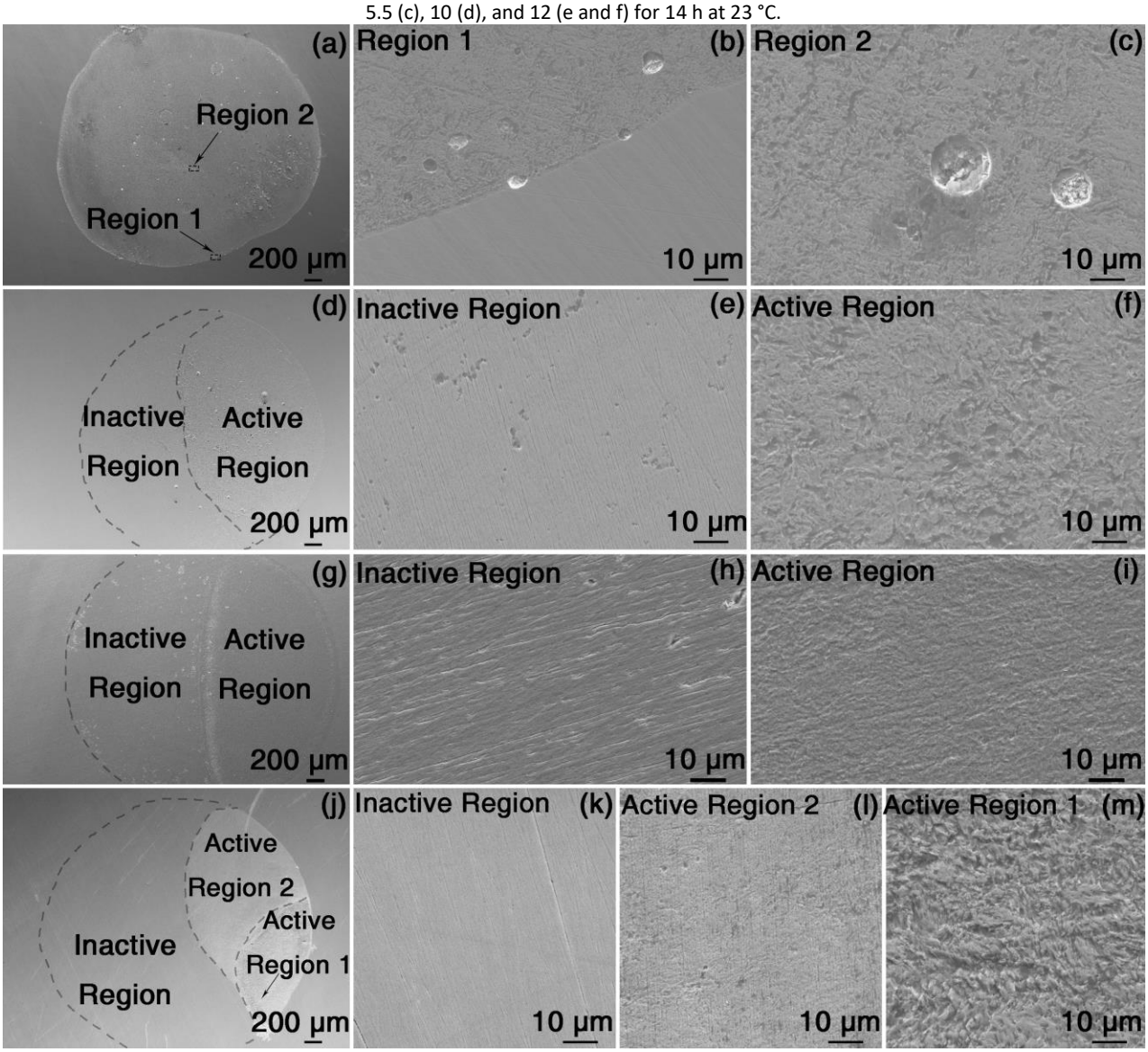

FIGURE 11. SEM SE images of the underlying corrosion attack after removal of corrosion products on the API-X100 pipeline steel specimens exposed beneath the oil covered 2 µL 1.7 mM NaCl droplets with initial pHs of 2 (a, b, and c), 4 (d, e, and f), 5.5 (g, h, and i), and 10 (j, k, l, and m) for 14 h at 23 °C.

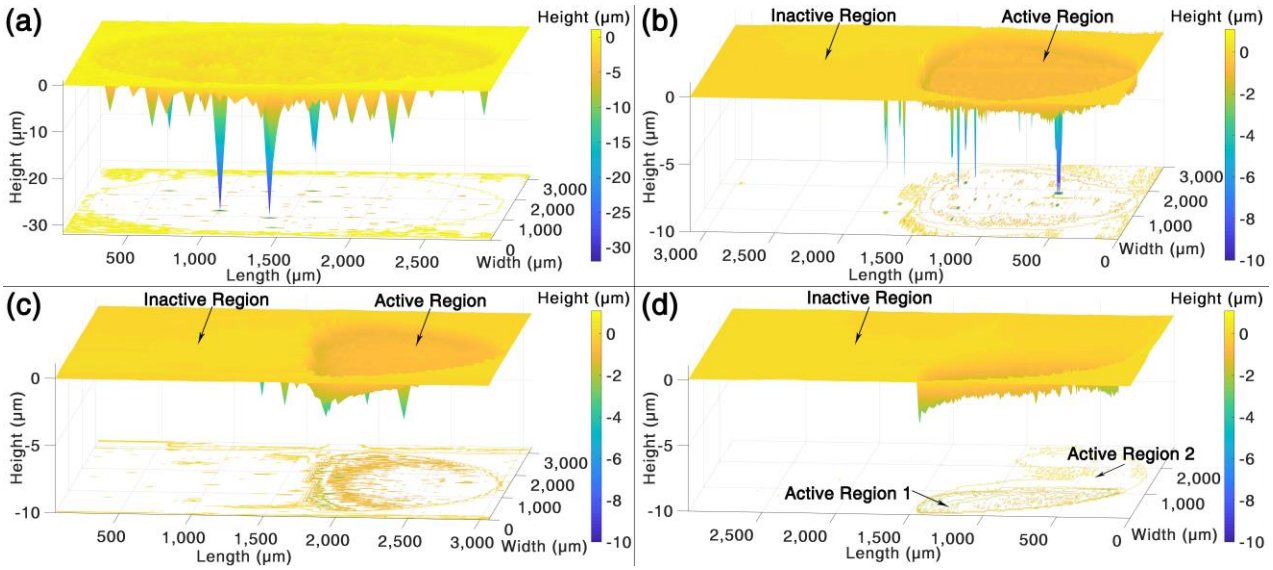

FIGURE 12. The three-dimensional morphologies of the corrosion attack after removal of corrosion products formed beneath oil covered 2 μL 1.7 mM NaCl droplets with initial pHs of 2 (a), 4 (b), 5.5 (c), and 10 (d) for 14 h at 23 °C.

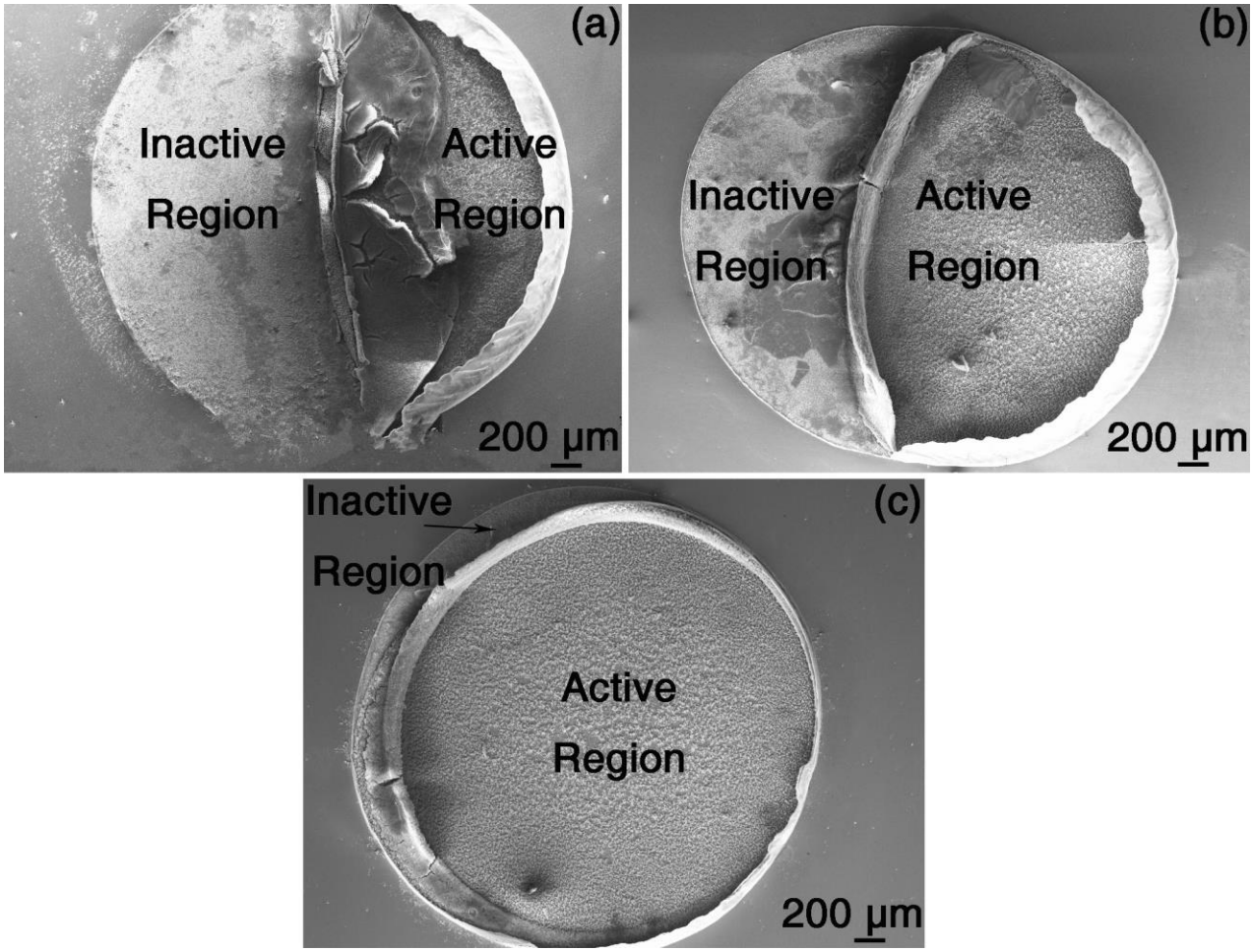

FIGURE 13. SEM SE images of API-X100 pipeline steel specimens exposed under oil covered 1.7 mM NaCl (a), 0.85 mM $CaCl_2$ (b), and 0.85 mM $MgCl_2$ (c) droplets with the volume of 2 μL for 14 h at 23 °C.

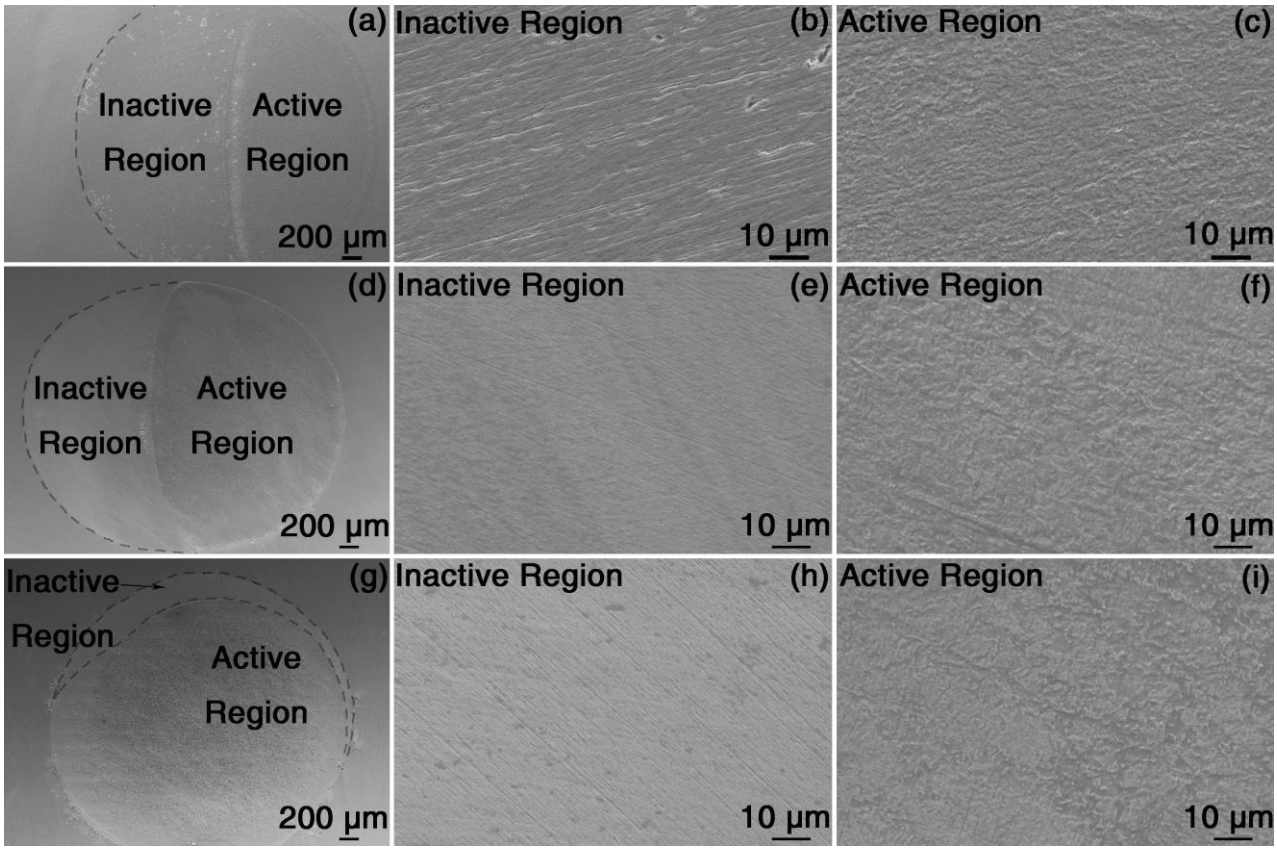

FIGURE 14. SEM SE images of the underlying corrosion attack after removal of corrosion products on the API-X100 pipeline steel specimens exposed beneath the oil covered 1.7 mM NaCl (a, b, and c), 0.85 mM $CaCl_2$ (d, e, and f), and 0.85 mM $MgCl_2$ (g, h, and i) droplets with the volume of 2 µL for 14 h at 23 °C.

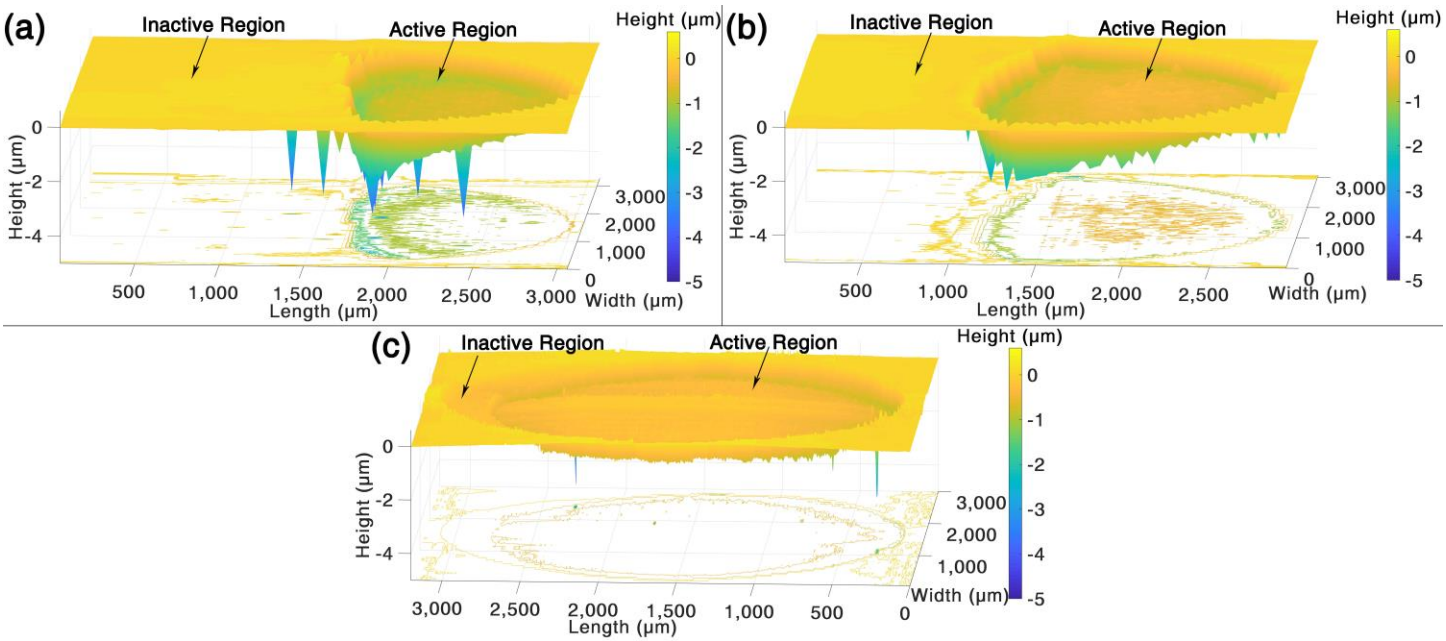

FIGURE 15. The three-dimensional morphologies of the corrosion attack after removal of corrosion products formed beneath oil covered 1.7 mM NaCl (a), 0.85 mM $CaCl_2$ (b) and 0.85 mM $MgCl_2$ (c) droplets with the volume of 2 µL for 14 h at 23 °C.

Tables

TABLE 1. Chemical composition of the API-X100 pipeline steel specimens.

Element	C	Ni	Cr	Mn	Nb	Al	Cu	Ti	V	Mo	Fe
X100 (wt.%)	0.1	0.13	0.016	1.66	0.043	0.02	0.25	0.02	0.003	0.19	Balance